OXFORD

Journal of Petrology, 2022, **63**, 1–13
https://doi.org/10.1093/petrology/egac084
Original Manuscript

A New Method for Relating Zircon Crystallisation to Petrogenetic Events

Laura A. Miller[1,*], Peter A. Cawood[1] and Andrew J. Berry[2]

[1]School of Earth, Atmosphere and Environment, Monash University, Melbourne, Victoria 3800, Australia
[2]Research School of Earth Sciences, Australian National University, Canberra, Australian Capital Territory 2601, Australia

*Corresponding author: E-mail: laura.miller@monash.edu

Abstract

The trace element contents of zircon can provide unique insights into tectonothermal events, however, interpreting these data and identifying correlations with specific magmatic/metamorphic events can be challenging. This limits our ability to construct temporally constrained petrogenetic histories of complex metamorphic terranes. Unlocking the information that the rare earth element (REE) patterns of zircon contain is difficult because of the need to quantify differences. We have parametrised the shape of zircon REE patterns in terms of three independent parameters: average abundance, slope, and curvature. Quantifying REE patterns using independent shape parameters is similar to the use of REE ratios but is an improvement as (1) it uses information from all 14 REE rather than just two; (2) the use of two independent parameters (e.g. slope and curvature) is a more robust discriminant than the use of a single ratio; and (3) subtle variations in shape are easily distinguished enabling trends in the REE patterns of large datasets to be identified. Quantitative models were constructed showing how the shapes of the REE patterns of zircon change due to the co-crystallisation of other metamorphic minerals (monazite, apatite, and garnet). Diagnostic changes in shape enable the REE contents of zircon crystals or crystal zones to be accurately related to the growth of specific minerals and hence metamorphic events. The results were used to interpret the REE patterns of zircons from high-grade metamorphic terranes, which have experienced multiple deformation events (Val Malenco, Italy; Betic Cordillera, Spain; Seram, Indonesia; Lewisian Gneiss Complex, Scotland; Napier Complex, East Antarctica) and clearly identified zircon that crystallised in the presence of garnet. Quantitative comparison enabled zircon that crystallised prior to, synchronously with, or after garnet to be identified. Similar models can be used to interpret the REE patterns of monazite. This allows the relative timing of the growth of these minerals to be accurately constrained, which given the importance of zircon for geochronology and garnet for geobarometry has the potential to provide insights into the evolution of a metamorphic event.

INTRODUCTION

Establishing the chronology and nature of igneous and metamorphic events that have affected the continental crust is key to understanding both the dynamics of current tectonic processes (e.g. Pownall *et al.*, 2014) and metamorphic events that deformed the early continental crust (e.g. Nutman *et al.*, 2002; Moyen, 2011; Reimink *et al.*, 2014). Metamorphic terranes have often experienced multiple events and have complex histories, whereby geochemical signatures may be overprinted or in some cases completely reset, limiting our ability to reconstruct their tectonothermal histories. Zircon is the exception to this, where igneous cores are often resistant to the effects of later metamorphic events. However, through partial recrystallisation, the growth of rims, or age resetting of crystal zones due to the loss of Pb, zircon can potentially reveal a level of chronological detail that matches the complexity of events. As a result zircon U–Pb dates have been, and continue to be, key to constructing geochronological histories of high-grade metamorphic terranes (e.g. Crowley *et al.*, 2006; Hopkins *et al.*, 2008).

Ancillary trace element data can be used to identify the type (e.g. igneous or metamorphic) and/or nature (e.g. grade of metamorphism) of an event associated with U–Pb dates (Burnham & Berry, 2017; Claiborne *et al.*, 2018). The Th/U ratio, Eu anomaly, and rare earth element (REE) contents of zircon are commonly used to characterise metamorphic events (Rubatto, 2017). The use of the REE has proven to be extremely successful, where simple qualitative assessment of changes in REE pattern shape (e.g. Whitehouse & Platt, 2003; Pownall *et al.*, 2019) and the use of ratios such as La/Sm or Yb/Gd to quantify differences in slope (e.g. Schaltegger *et al.*, 1999; Rubatto, 2002; Kelly & Harley, 2005; Taylor *et al.*, 2017) have enabled detailed tectonothermal histories to be constructed. However, the qualitative assessment of REE pattern shape is subjective while the use of some REE ratios can be affected by light REE (LREE) contamination (a problem that particularly affects zircon due to its naturally low LREE contents and tendency to host LREE-rich inclusions of monazite and apatite; Burnham, 2020), analytical artefacts such as oxide interferences, and mid-REE (MREE) and heavy REE (HREE) 'wobbles' (O'Neill, 2016). This means that the relationship between dates and processes inferred from REE data can be ambiguous. This problem is accentuated for detrital and xenocrystic zircons, and zircons that record metamorphic events that have since been overprinted in their host rock, as detailed petrographic observations cannot inform the interpretation.

Here, we present a new way of interpreting the REE patterns of zircons in terms of the metamorphic events that they record.

Received: October 25, 2021. **Revised:** July 22, 2022. **Accepted:** August 8, 2022

Zircon REE concentrations can be fitted to orthogonal polynomials to obtain three independent parameters (average concentration, slope, and curvature) that quantify the shape of the pattern (O'Neill, 2016; Anenburg, 2020). This approach allows subtle differences in REE pattern shape to be identified. For example, when the curvature of a REE pattern is plotted against its slope, mid-ocean ridge basalts, and ocean island basalts define different fields (O'Neill, 2016). It is also possible to model the effect of petrogenetic processes (e.g. fractional crystallisation and partial melting) on the different shape components of a REE pattern (O'Neill, 2016), allowing processes to be inferred from changes in pattern shape (Miller *et al.*, 2022). Here, we model how the REE patterns of zircon and monazite are affected if crystallisation occurred in the presence of other REE-incorporating phases (e.g. garnet, allanite, and apatite). We test these models using zircon and monazite populations that are considered to have crystallised synchronously with garnet. The zircon populations selected are from Val Malenco, Italy (Hermann & Rubatto, 2003), the Betic Cordillera, Spain (Whitehouse & Platt, 2003), Seram, Indonesia (Pownall *et al.*, 2019), the Lewisian Gneiss Complex, Scotland (MacDonald *et al.*, 2015), and the Napier Complex, East Antarctica (Hokada & Harley, 2004; Taylor *et al.*, 2017), and the monazite populations from Val Malenco, Italy (Hermann & Rubatto, 2003), Mount Stafford, Australia (Rubatto *et al.*, 2006), and the Himalayas, Bhutan (Warren *et al.*, 2018).

Fitting REE patterns

The geochemical behaviour of most of the REE is controlled by the decrease in ionic radius with increasing atomic number for a constant charge (3+). Consequently, chondrite (CI) normalised REE patterns vary smoothly as a function of REE radii (r_{REE}) and can be fitted to orthogonal polynomials that are derived from the radii (O'Neill, 2016). The obvious exceptions to this rule are Ce and Eu, which can occur as Ce^{4+} and Eu^{2+}, and these REE should be excluded from the fit if either are present (Burnham & Berry, 2012). Orthogonal polynomials are used to ensure that the coefficients of the polynomials vary independently of each other, although this is only strictly true if the same number of REE are used in the fit as used to derive the polynomials. The orthogonal polynomials used here (given in Tables 1 and 2 of O'Neill, 2016) were derived from the radii of 13 of the REE with Eu excluded. For zircon, where La is commonly contaminated by LREE-rich inclusions and Ce anomalies are ubiquitous, it would be appropriate to derive new polynomials excluding La, Ce, and Eu, which are given in Table S1. There was little difference in the coefficients (λ_n) obtained from fits using these polynomials and those of O'Neill (2016), and hence the latter were preferred to enable comparison with previously published λ_n values and avoid confusion in the literature. The fit of the orthogonal polynomials to a REE pattern can be written as (O'Neill, 2016; Fig. 1):

$$\ln\left([\mathrm{REE}]/[\mathrm{REE}]_{\mathrm{CI}}\right) = \lambda_0 {f_0}^{\mathrm{orth}} + \lambda_1 {f_1}^{\mathrm{orth}} + \lambda_2 {f_2}^{\mathrm{orth}} + \lambda_3 {f_3}^{\mathrm{orth}} + \lambda_4 {f_4}^{\mathrm{orth}} + etc., \quad \text{Eq. 1}$$

where $[REE]/[REE]_{CI}$ refers to the REE CI normalised abundances, ${f_n}^{orth}$ to the orthogonal polynomials, and λ_n to the coefficients of the orthogonal polynomials, where n is the order of polynomial. Example fits to zircon REE patterns are shown in Fig. 1, noting that abundances are given as $\log_e$ to be consistent with the orthogonal polynomial fitting space (see Appendix 1 of O'Neill, 2016) rather than $\log_{10}$ as more commonly reported. The orthogonal polynomials describe different shape components, shown in Fig. 1e–h, where ${f_0}^{orth}$ is a constant function (black), ${f_1}^{orth}$ a linear function (red), ${f_2}^{orth}$ a quadratic function (blue), and ${f_3}^{orth}$ a cubic function (green). The cubic and higher-order functions commonly reflect nothing more than 'noise' in a REE pattern, with most of the variation in the pattern shape being captured by ${f_0}^{orth}$, ${f_1}^{orth}$, and ${f_2}^{orth}$ (O'Neill, 2016). The coefficients (λ_n) of the orthogonal polynomials parametrise the contribution of each polynomial to the shape of the REE pattern, where λ_0 is the average REE concentration of the pattern (i.e. the y intercept of the constant function; $\lambda_0 = 3.9$ in Fig. 1e and 2.0 in Fig. 1f), λ_1 the slope of the pattern (i.e. the gradient of the linear function; $\lambda_1 = -45$ in Fig. 1e and -14 in Fig. 1f; noting that ${f_1}^{orth}$ is negative) and λ_2 the curvature of the pattern (i.e. the openness or tightness and upward or downward opening of the quadratic function; $\lambda_2 = -9$ in Fig. 1e and -260 in Fig. 1f). Thus, by fitting a REE pattern to the orthogonal polynomials the information represented by the 14 REE contents is minimised to three main shape components (λ_0, λ_1, and λ_2). Further, the deviation of Ce or Eu contents from the fit (i.e. $\Sigma\lambda_n f_n$) allows the Ce and Eu anomalies to be accurately quantified.

Partition coefficients D^{REE} are also smooth functions of r_{REE} and can be fitted to the same orthogonal polynomials (Fig. S1):

$$D^{\mathrm{REE}} = \delta_0 {f_0}^{\mathrm{orth}} + \delta_1 {f_1}^{\mathrm{orth}} + \delta_2 {f_2}^{\mathrm{orth}} + \delta_3 {f_3}^{\mathrm{orth}} + \delta_4 {f_4}^{\mathrm{orth}} + etc., \quad \text{Eq. 2a}$$

where the δ_n coefficients describe the shape of the REE partitioning pattern (in the same way that λ_n describe the shape of a REE pattern). The bulk partition coefficients of the REE ($\overline{D}^{REE}$, given by $\Sigma D^{REE} m_x$), where D^M is the crystal/residual partition coefficient and m_x the mass fraction of crystalline phase x, can also be fitted to give

$$\overline{D}^{\mathrm{REE}} = \bar{\delta}_0 {f_0}^{\mathrm{orth}} + \bar{\delta}_1 {f_1}^{\mathrm{orth}} + \bar{\delta}_2 {f_2}^{\mathrm{orth}} + \bar{\delta}_3 {f_3}^{\mathrm{orth}} + \bar{\delta}_4 {f_4}^{\mathrm{orth}} + etc. \quad \text{Eq. 2b}$$

MODELLING

The absolute and relative amounts of the REE in zircon will be affected by the co-crystallisation of other REE incorporating minerals. This has been shown to clearly be the case when zircon crystallises alongside garnet (e.g. Rubatto, 2002). The aim of the modelling was to investigate how the shape of the REE pattern of zircon, and other minerals, would respond to the changing availability of the REE in the bulk system due to the crystallisation of other phases that compete for the REE. The modelling was performed in two stages. Firstly, the change in the REE pattern of the bulk system due to the crystallisation of different REE bearing phases was modelled. Then, the REE pattern of zircon (λ_n^{xtl}) crystallising from that system was predicted. We hereafter refer to the bulk system that remains after the crystallisation of REE-bearing phases as the residual.

Equations

The effect of crystallisation on the concentration of an element in a residual can be modelled using the standard equation for fractional crystallisation (e.g. Shaw, 2006):

$$\ln\left([M_{res}]/[M_0]\right) = \ln(F)(\overline{D}^{M} - 1), \quad \text{Eq. 3a}$$

where $[M_{res}]$ is the concentration of element M in the residual, $[M_0]$ the initial concentration, and F a measure of the degree of crystallisation (which varies between 0 and 1, where 1 corresponds to no crystallisation). Combing Equation (2b) with

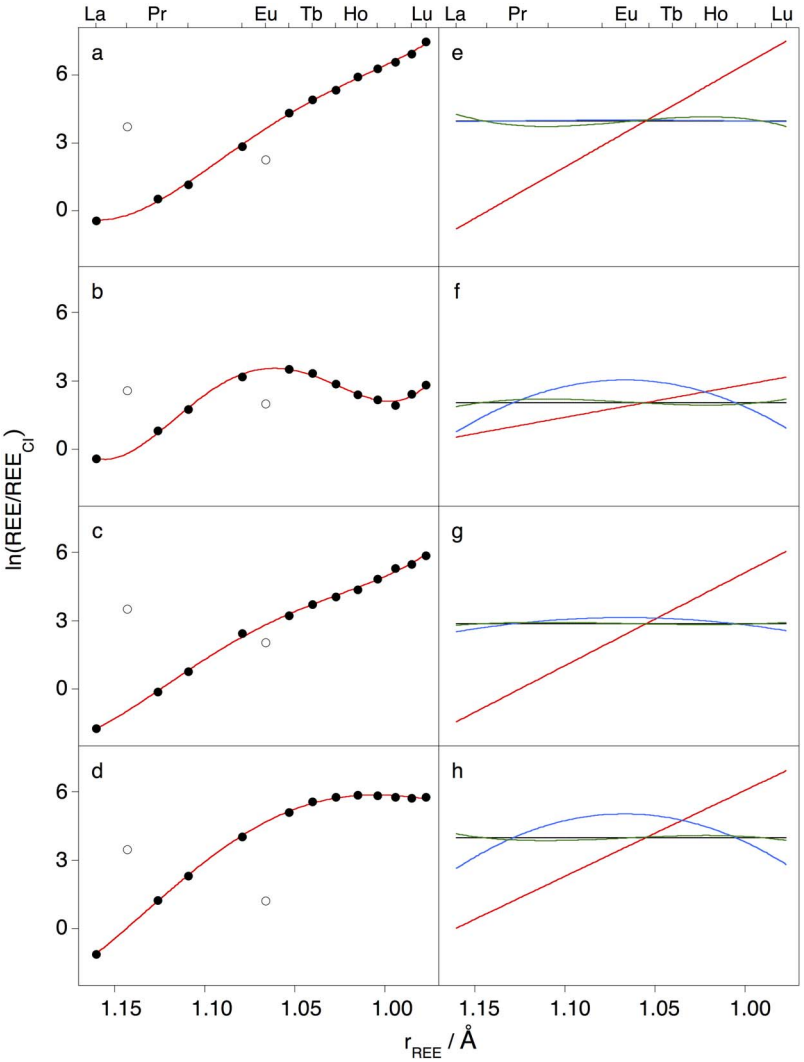

Fig. 1. Example natural log (ln; log$_e$) CI normalised abundances of the REE (symbols), as a function of ionic radius (r_{REE}), and fit (red line) for zircons from (a) and (b) the Betic Cordillera, Spain, (a) not associated with garnet growth (core G5B) and (b) associated with garnet growth (rim G1), and (c) and (d) from the Lewisian Gneiss Complex, (c) not associated with garnet growth (GMBP04Z2-1) and (d) associated with garnet growth (GM23Z6-2), and (e–h) the corresponding orthogonal polynomials that sum to give the fits in (a–d), $\lambda_0 f_0$ (average abundance; black), $\lambda_1 f_1$ (slope; red), $\lambda_2 f_2$ (curvature; blue), and $\lambda_3 f_3$ (cubic function; green). REE not included in the fits (Ce and Eu) are shown by open symbols. The data for each sample are given in Supplementary Table S2. In (e–h) the value of λ_0 has been added to the $\lambda_1 f_1$, $\lambda_2 f_2$, and $\lambda_3 f_3$ polynomials for ease of plotting. The cubic component is so small that $\lambda_3 f_3$ overlies $\lambda_0 f_0$.

Equation (3a) gives

$$\Psi_0{}^{\Delta res} = \ln(F)\,(\bar{\delta}_0 - 1)\,,\ \Psi_1{}^{\Delta res} = \ln(F)\,(\bar{\delta}_1)\,,\ \Psi_2{}^{\Delta res} = \ln(F)\,(\bar{\delta}_2)\,, \quad \text{Eq. 3b}$$

where $\Psi_n{}^{\Delta res}$ are termed petrogenetic process vectors (O'Neill, 2016). These process vectors describe the change in average REE abundance ($\Psi_0{}^{\Delta res}$), slope ($\Psi_1{}^{\Delta res}$), and curvature ($\Psi_2{}^{\Delta res}$) between the final and initial REE patterns:

$$\ln(M_{res}/M_0) = \ln(M_{res}) - \ln(M_0) \quad \text{Eq. 4}$$

and

$$\Psi_0{}^{\Delta res} = \lambda_0{}^{res} - \lambda_0{}^0,\ \Psi_1{}^{\Delta res} = \lambda_1{}^{res} - \lambda_1{}^0,\ \Psi_2{}^{\Delta res} = \lambda_2{}^{res} - \lambda_2{}^0, \quad \text{Eq. 5}$$

where $\lambda_n{}^{res}$ describe the shape of the REE pattern of the residual and $\lambda_n{}^0$ the shape of the initial system. Thus, Equation (3b) enables changes in the λ_n of the residual system due to fractional crystallisation to be modelled. To compare a process for different starting compositions, the vectors $\Psi_n{}^{\Delta res}$ can be determined for the process and then transposed in λ_n space by the addition of the initial REE pattern ($\Psi_n{}^{\Delta res} + \lambda_n{}^0 = \lambda_n{}^{res}$; Equation (5)). Similarly, to compare different processes for the same starting composition, the vectors $\Psi_n{}^{\Delta res}$ can be determined for each process and then transposed to the λ_n of the starting composition.

Analogous equations can be obtained to model the λ_n of the fractionating crystal:

$$\ln([M_{xtl}]/[M_0]) = \ln(F)(\overline{D}^M - 1) + \ln(\overline{D}^M) \quad \text{Eq. 6a}$$

$$\Psi_0{}^{\Delta xtl} = \ln(F)\,(\bar{\delta}_0 - 1) + \bar{\delta}_0{}^*,\ \Psi_1{}^{\Delta xtl} = \ln(F)\,(\bar{\delta}_1) + \bar{\delta}_1{}^*,\ \Psi_2{}^{\Delta xtl} = \ln(F)\,(\bar{\delta}_2) + \bar{\delta}_2{}^*, \quad \text{Eq. 6b}$$

where $[M_{xtl}]$ is the concentration of element M in the fractionating crystal, $\bar{\delta}_n*$ are obtained by fitting $\ln\overline{D}^{REE}$ patterns (in the same way as $\bar{\delta}_n$ are obtained by fitting D^{REE} patterns), and $\Psi_n{}^{\Delta xtl}$ describe

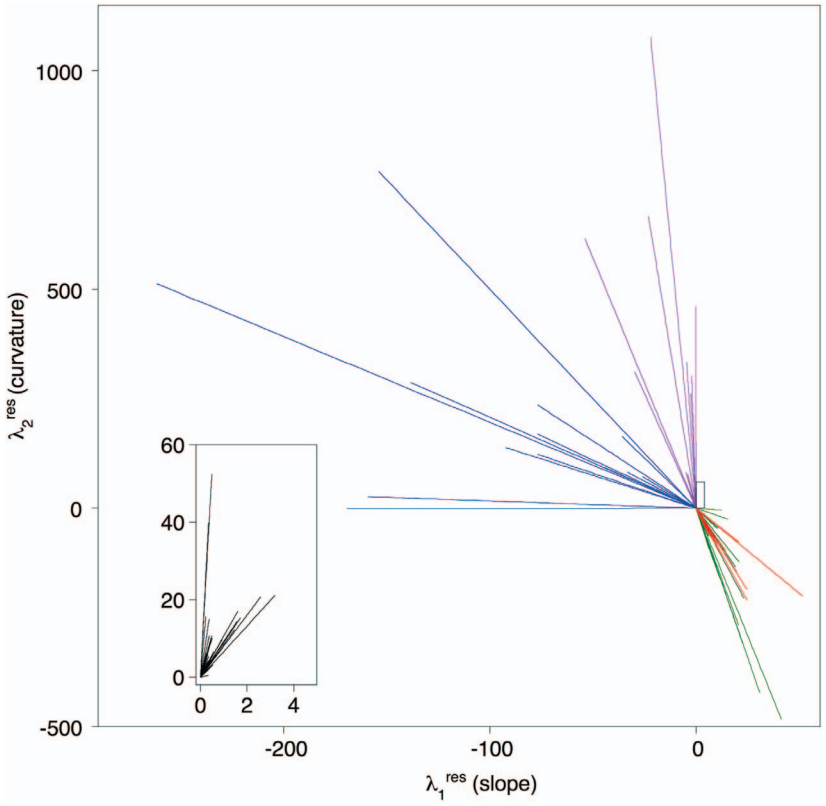

Fig. 2. Modelled changes in λ_2^{res} (curvature) and λ_1^{res} (slope) of the REE pattern of a residual system (vectors) caused by 5% crystallisation of garnet (red), zircon (green), monazite (blue), apatite (purple), and amphibole (inset; black) for different values of D^{REE} (Supplementary Data). All vectors start at $\lambda_1^{res} = \lambda_2^{res} = 0$, arrowheads are not shown for clarity. Vectors with anomalously large magnitude are not shown.

the changes in the REE pattern of the fractionating crystal as a function of the amount of crystallisation. The petrogenetic process vectors $\Psi_n^{\Delta xtl}$ can also be written as

$$\Psi_0^{\Delta xtl} = \lambda_0^{xtl} - \lambda_0^0, \Psi_1^{\Delta xtl} = \lambda_1^{xtl} - \lambda_1^0, \Psi_2^{\Delta xtl} = \lambda_2^{xtl} - \lambda_2^0, \quad \text{Eq. 7}$$

where λ_n^{xtl} is the shape of the REE pattern of the fractionating crystal.

The change in REE pattern shape as a function of the degree of crystallisation can also be determined using Equation (3a) for the residual and Equation (6a) for the fractionating crystal. The resulting difference patterns can then be fit to the orthogonal polynomials to determine the change in λ_n^{res} ($\Psi_n^{\Delta res}$) and λ_n^{xtl} ($\Psi_n^{\Delta xtl}$) due to fractional crystallisation. This method is more time consuming as it requires fitting many REE patterns, rather than a single fit of the partition coefficients, to the orthogonal polynomials. However, as this method may be more intuitive, and as sometimes it is not possible to transpose a petrogenetic equation into δ_n space (e.g. batch melting) the approach is demonstrated in Worked Examples 1 and 2 (Supplementary Information).

Residual system models

The effect of the crystallisation of different minerals on the REE pattern of the residual system was modelled first. The most important REE hosting phases in the majority of metamorphic rocks are allanite, amphibole, apatite, garnet, monazite, and zircon. These minerals all have different D^{REE}. Further, there is a range in D^{REE} for any one mineral as D^{REE} are affected by differences in pressure, temperature, and mineral and melt composition (Wood & Blundy, 2014). Thus, to investigate the variation in shape of the D^{REE} pattern for a given mineral, partition coefficients determined for a range of conditions were selected from the literature. To compare the shape of D^{REE} patterns (i.e. δ_n) for different minerals, partition coefficients that had been determined for similar compositions, temperatures, and pressures were selected. The D^{REE} were fit to Equation (2a) to determine the δ_n coefficients. The D^{REE} and the δ_n coefficients are given in the Supplementary Data.

The terms describing the shape of the D^{REE} patterns (δ_n) were substituted into Equation (3b) to model changes in the REE pattern of the residual system ($\Psi_n^{\Delta res}$) caused by fractional crystallisation (Worked Example 1 in Supplementary Information). Petrogenetic process vectors ($\Psi_n^{\Delta res}$ or $\Delta\lambda_n$; Equation (5)) were calculated using D^{REE} determined for a range of conditions (pressure, temperature, and melt composition) for the crystallisation of amphibole, apatite, garnet, monazite, and zircon and are shown in Fig. 2. A subset of these, corresponding to D^{REE} determined for different minerals at the same conditions, is shown in Fig. 3. A further subset, corresponding to the crystallisation of garnet during cooling using D^{REE} determined at different temperatures is shown in Fig. 4b. The degree of crystallisation strongly affects the magnitude of the vectors (O'Neill, 2016) and to facilitate comparison of relative magnitudes all of the vectors shown in Fig. 2 were calculated for 5% crystallisation, and 1% crystallisation intervals are indicated by markers on the vectors shown in Figs 3 and 4. The REE patterns of the residual system after discrete fractions of garnet and monazite crystallisation, which correspond to λ_1^{res} and λ_2^{res} points on the garnet and monazite vectors in Fig. 3, were generated and are shown in Fig. 5a and c (the slope and curvature polynomial components are shown in Figs S2 and S3). The vectors

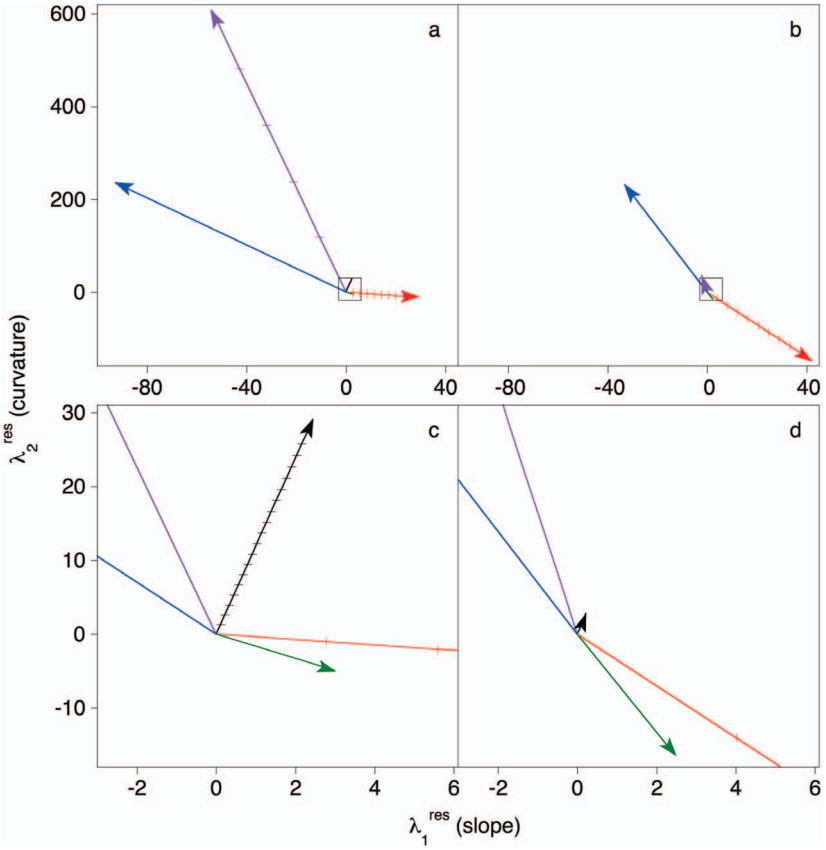

Fig. 3. Modelled changes in λ_2^{res} (curvature) and λ_1^{res} (slope) of the REE pattern of the residual system (vectors) caused by crystallisation of 10% garnet (red), 1% zircon (green), 1% monazite (blue), 5% apatite (purple), and 20% amphibole (black) using D^{REE} determined for granitic compositions at 1 GPa and ~ (a) 800 °C and (b) 1000 °C. The insets in (a) and (b) are shown in (c) and (d), respectively. 1% crystallisation intervals (the % of the bulk system that has crystallised to form the mineral) are marked and arrowheads show the direction of each vector.

(Figs 2 and 3) and the corresponding REE patterns (Fig. 5a and c) were generated from flat initial REE patterns such that the shape coefficients of the patterns are equivalent to the process vector or change in pattern shape (where $\Psi_n^{\Delta res} = \lambda_n^{res}$ when $\lambda_n^0 = 0$; Equation (5)).

Zircon models

The shapes of the REE patterns of zircon crystallising from the modelled systems were then derived using Equation (6b) (Worked Example 2 in Supplementary Information). The zircon λ_1^{xtl} and λ_2^{xtl} were modelled for 1% zircon crystallisation. The λ_1^{xtl} and λ_2^{xtl} for zircon crystallising alongside garnet and monazite are shown in Fig. 4a and the corresponding REE patterns are shown in Fig. 5b and d (the slope and curvature polynomial components are shown in Figs S2 and S3).

RESULTS

Changes in the residual system

The average partition coefficient (δ_0) relates to the enrichment or depletion of REE in the residual (λ_0^{res}). All of the minerals considered here (garnet, monazite, allanite, apatite, amphibole, and zircon) cause an overall depletion of the REE in the residual ($\delta_0 > 1$; Table S2). Thus, changes in λ_0^{res} (and λ_0^{xtl}) cannot be used to accurately distinguish between the crystallisation of these minerals, but they could be used to distinguish between these minerals and those in which the REE are incompatible (e.g. quartz, feldspar). Although of limited direct use, changes in λ_0^{res} should be consistent with crystallisation models inferred from changes in $\lambda_{1,2}^{res}$.

The crystallisation of amphibole causes an increase in λ_1^{res}, apatite causes little change to a moderate decrease in λ_1^{res}, while monazite causes a large decrease in λ_1^{res} (Fig. 2). A decrease in λ_1^{res} corresponds to an increasingly positive slope (Fig. 5c; the slope component is shown in Fig. S3c), which is consistent with preferential uptake of the LREE relative to the HREE by monazite and apatite, and an increasing depletion of the LREE relative to the HREE in the residual. The crystallisation of amphibole, apatite, and monazite all cause an increase in λ_2^{res} (Fig. 2). An increase in λ_2^{res} corresponds to an increasingly negative quadratic function (Fig. 5c; the curvature component is shown in Fig. S3e). Mainly due to their different effects on λ_1^{res} the vectors for amphibole, apatite, and monazite each define a 'field' of directions that is mineral specific (Fig. 2). Both garnet and zircon cause an increase in λ_1^{res} and a decrease in λ_2^{res} (red and green vectors; Fig. 2). An increase in λ_1^{res} corresponds to an increasingly negative slope and a decrease in λ_2^{res} corresponds to an increasingly positive quadratic function (Fig. 5a; the slope and curvature components are shown in Fig. S2c and e). An increasingly negative slope is consistent with preferential uptake of the HREE relative to the LREE causing a depletion of the HREE relative to the LREE in the residual.

The vectors for allanite are not shown in Figs 2 and 3 as the vectors determined using phenocryst-matrix D^{REE} have a different direction (190°) to those determined using experimental D^{REE} (350°; Supplementary Data). The difference in vector direction

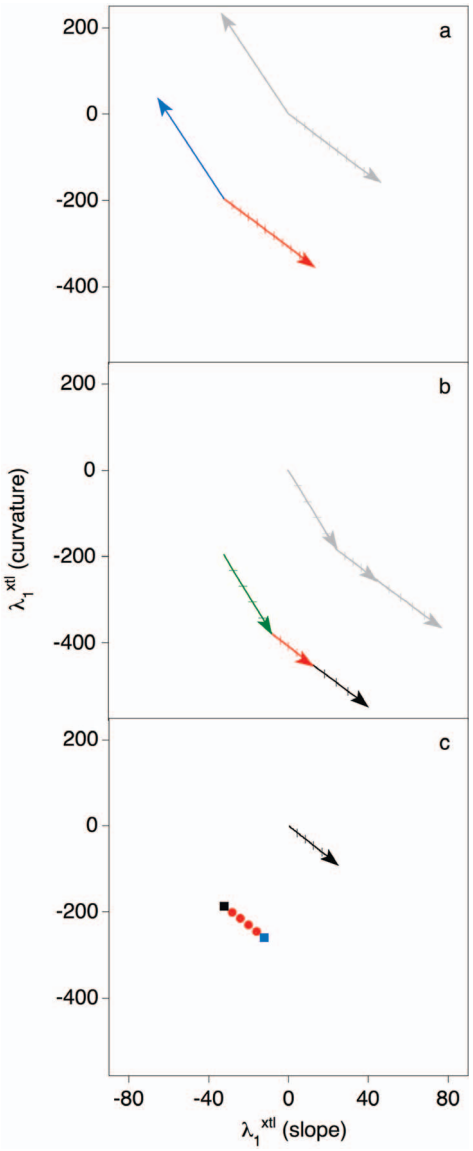

Fig. 4. Modelled changes in λ_2^{xtl} (curvature) and λ_1^{xtl} (slope) of the REE pattern of zircon that crystallised (a) simultaneously with either garnet (red) or monazite (blue), (b) simultaenously with garnet while the system is cooling from 1000 °C (green), to 950 °C (red) to 900 °C (black), (c) prior to (black square), simultaenously with (red symbols) and after (blue square) garnet (black vector). 1% crystallisation intervals are marked and arrowheads show the direction of the vectors. The grey vectors in (a) and (b) correspond to the residual.

could be due to the different conditions at which the partitioning occurred, or the phenocrysts and matrix may not have been in equilibrium. The number of D^{REE} for allanite is limited, and hence it is difficult to establish the effect of allanite crystallisation.

The vectors for monazite and apatite generally have a larger magnitude (or length) than the vectors for the crystallisation of garnet, zircon, and amphibole (Figs 2 and 3). Monazite and apatite strongly partition the LREE over the HREE, which results in a large change in the slope and curvature of the residual system. In contrast, amphibole weakly fractionates the REE and thus only causes small changes to the slope and curvature of the residual (Figs 2 and 3). Zircon and garnet cause similar changes to λ_1^{res} and λ_2^{res} (Figs 2 and 3), and in this case, it is important to consider the expected amount of crystallisation. The growth of metamorphic zircon is severely limited by the availability and diffusion of Zr and more than 1% zircon is unlikely (Yakymchuk & Brown, 2014), whereas substantial amounts (>20%) of metamorphic garnet can crystallise. This means that the magnitude of changes in λ_1^{res} and λ_2^{res} caused by the crystallisation of zircon is unlikely to be discernible, whereas the change caused by garnet could be large (Fig. 3).

If more than one mineral crystallised at the same time then the direction and magnitude of the petrogenetic process vector would be represented by the sum of the vectors corresponding to each mineral. The vector sum is strongly weighted by the magnitudes of the vectors, for example, if a system was crystallising 10% garnet and 90% amphibole the vector sum would essentially have the same direction as the garnet vector. Thus, the crystallisation of minerals that incorporate large amounts of the REE, and hence have large magnitude vectors (e.g. monazite), will control trends in λ_1^{res} and λ_2^{res}, with directional contributions caused by phases containing a small proportion of the total REE budget being insignificant.

The vectors for the crystallisation of different minerals over a range of conditions (pressure, temperature, and melt composition) have directions that are characteristic of the mineral crystallising (Figs 2 and 3). The vectors for garnet, zircon, monazite, apatite, and amphibole have the same relative directions at different temperatures (e.g. 1000 °C, Fig. 3a and c; 800 °C, Fig. 3b and d), while the vectors for the crystallisation of garnet during cooling (1000 to 900 °C), all have the same general direction (Fig. 4b). This indicates that the strongest control on the slope and curvature of a REE pattern, and thus vector direction, is mineralogical, with changes in pressure, temperature, and melt composition resulting in second-order perturbations on the trend defined by each mineral (Figs 2 and 3). The magnitude of the vectors is also characteristic of the mineral crystallising (Figs 2 and 3). This is a product of both the absolute REE compatibilities in the mineral and the degree to which the mineral fractionates the REE.

Zircon crystallisation

The λ_1^{xtl} and λ_2^{xtl} of zircon are offset from the λ_1^{res} and λ_2^{res} of the system from which it crystallises. This offset is a result of the differential uptake of the REE giving a zircon REE pattern with a steep slope and large downward curvature (a system with λ_1^{res}, $\lambda_2^{res} = 0$, 0 crystallises zircon with λ_1^{xtl}, $\lambda_2^{xtl} = \sim -32, -200$; Figs 4, 5a and b). The size of the offset is dependent on the amount of zircon crystallisation and the shape of the D^{REE} used (see Equation (6a)). As all models used the same amount of zircon crystallisation (1%) and the same D^{REE} the offset is constant in the example shown in Fig. 4. As such, the slope and curvature of the different zircon growths (crystallisation intervals; Fig. 4) define trends that are parallel to those of the system from which they crystallised. Accordingly, the zircon REE patterns shown in Fig. 5b show the same change in slope and curvature as the residual patterns (Fig. 5a) but superimposed on the initial shape of the zircon REE pattern (Figs 5a and b, S2, and S4).

The direction and magnitude of changes in λ_1^{res} and λ_2^{res} of a residual system caused by the crystallisation of different REE-bearing minerals is characteristic of each mineral (Figs 2 and 3). As the λ_1^{xtl} and λ_2^{xtl} of zircon mimics the changes in the λ_1^{res} and λ_2^{res} of the residual (Fig. 4), the characteristic changes caused by the crystallisation of specific REE-bearing minerals means that the λ_1^{xtl} and λ_2^{xtl} of zircon can be used to identify the crystallisation of these minerals.

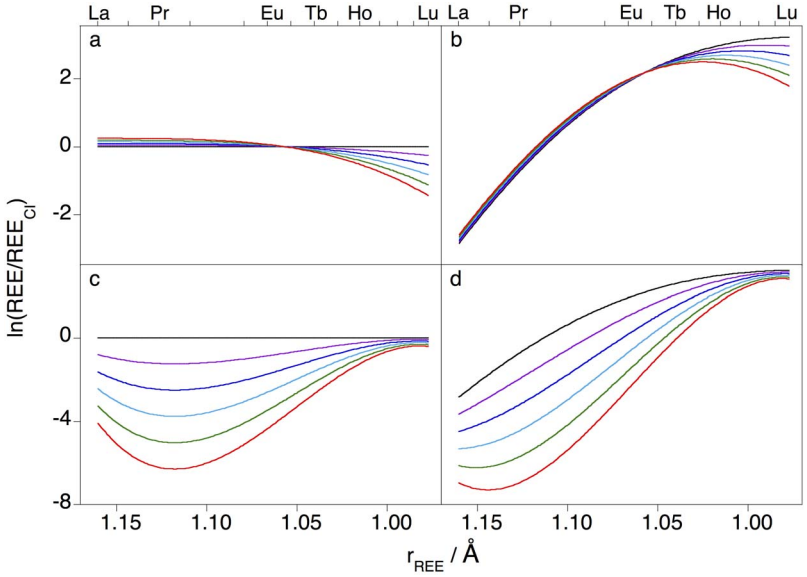

Fig. 5. Modelled REE pattern shapes, as a function of ionic radius ($r_{REE,}$), of (a) a system (black) that crystallised 4% (purple), 8% (dark blue), 12% (light blue), 16% (green), and 20% (red) garnet, and (b) 1% zircon crystallising from that system, (c) a system (black) that crystallised 0.2% (purple), 0.4% (dark blue), 0.6% (light blue), 0.8% (green), and 1% (red) monazite and (d) 1% zircon crystallising from that system. To emphasise the change in shape the initial REE patterns in (a) and (c) were chosen to be flat.

Timing of crystallisation

The shape of the REE pattern of a residual system continuously changes while garnet is crystallising (Figs 4c and 5a). As a result, each new growth or overgrowth of zircon that crystallises synchronously with garnet from that residual has different λ_1^{xtl} and λ_2^{xtl}, where the differences in λ_1^{xtl} and λ_2^{xtl} correspond to the differences in λ_1^{res} and λ_2^{res}. This means that the λ_1^{xtl} and λ_2^{xtl} of multiple growths of zircon that crystallise synchronously with garnet will define a linear trend that is parallel to the petrogenetic process vector for garnet (Fig. 4c). In contrast, the λ_1^{res} and λ_2^{res} of the system will remain essentially constant during the crystallisation of zircon that forms after the crystallisation of garnet such that the λ_1^{xtl} and λ_2^{xtl} of the new zircon growths will be similar. The modelling shows the λ_1^{xtl} and λ_2^{xtl} of zircon that crystallised after garnet as a point (blue square; Fig. 4c); however, in reality, the λ_1^{xtl} and λ_2^{xtl} of multiple zircon growths crystallising from the same system are likely to be represented by a 'group' or 'cluster' (it is rare for the REE patterns of zircons to be exactly the same). This 'group' will be separated from the λ_1^{xtl} and λ_2^{xtl} of zircon that crystallised prior to the crystallisation of garnet in the direction of the garnet crystallisation vector (Fig. 4c). Thus, the relative positions of the λ_1^{xtl} and λ_2^{xtl} of multiple zircon growths can be used to determine the relative timing of crystallisation, where synchronous crystallisation forms trends parallel to that of the residual system and temporally separated crystallisation forms spatially separated but vector-linked groups.

DISCUSSION

The characteristic changes in REE pattern shape caused by specific minerals and the relative values of the slope (λ_1^{xtl}) and curvature (λ_2^{xtl}) of different growths of zircon (which define groups or trends) means that it should be possible to identify minerals that crystallised prior to, synchronously with, or post crystallisation of zircon(s). To investigate this further, we determined the λ_n^{xtl} of zircons from metamorphic terranes and interpreted them in terms of the modelled vectors.

Zircon populations that have multi-phase histories where the chronology of events has been determined through detailed petrographic observations were selected to test the modelling. The zircons all exhibit metamorphic rims that have different U–Pb ages and distinct trace element contents. The rims are thought to have crystallised (1) from partial melts that had previously crystallised garnet (Val Malenco; Hermann & Rubatto, 2003), (2) synchronously with garnet under conditions close to partial melting (Betic Cordillera; Whitehouse & Platt, 2003), and (3) in the presence of garnet (Seram, Pownall *et al.*, 2019). In these studies, the signature of garnet in the zircon REE patterns was identified through qualitative comparisons of zircon REE pattern shapes and the use of REE ratios. Zircon populations from the Lewisian Gneiss Complex, Scotland (MacDonald *et al.*, 2015) and the Napier Complex, East Antarctica (Hokada & Harley, 2004; Taylor *et al.*, 2017) were also selected. Both are Archean crustal fragments with complex tectonothermal histories (e.g. Sutton & Watson, 1951; Kelly & Harley, 2005; Wheeler *et al.*, 2010; Goodenough *et al.*, 2013; Kusiak *et al.*, 2013). The REE data used are reproduced from their original sources in Table S2.

The REE patterns of the zircon populations were fit to the orthogonal polynomials (Equation 1) and the λ_n^{xtl} are given in Table S2. Example fits are shown in Figs 1 and S5. The REE patterns of the zircon rims from the Betic Cordillera, Spain, have significant cubic components (Fig. 1b). A large cubic contribution can be produced in zircon REE patterns when it crystallises alongside garnet (Fig. S4). To assess the quality of the fits, the reduced χ^2 were determined using a constant uncertainty of 0.1 for the natural logarithm of the CI normalised REE values. This uncertainty was assigned to all data as many of the datasets did not report errors for the analyses, while the use of the same error means that χ^2 values can easily be compared between datasets. However, the assignment of an error means that $\chi^2 > 1$ can indicate that the error has been underestimated (similarly $\chi^2 < 1$ that the error has been overestimated) rather than that the fits or model are poor. Thus, the values of χ^2 were not used to exclude REE patterns due to a poor fit but rather to allow the reliability of trends in the

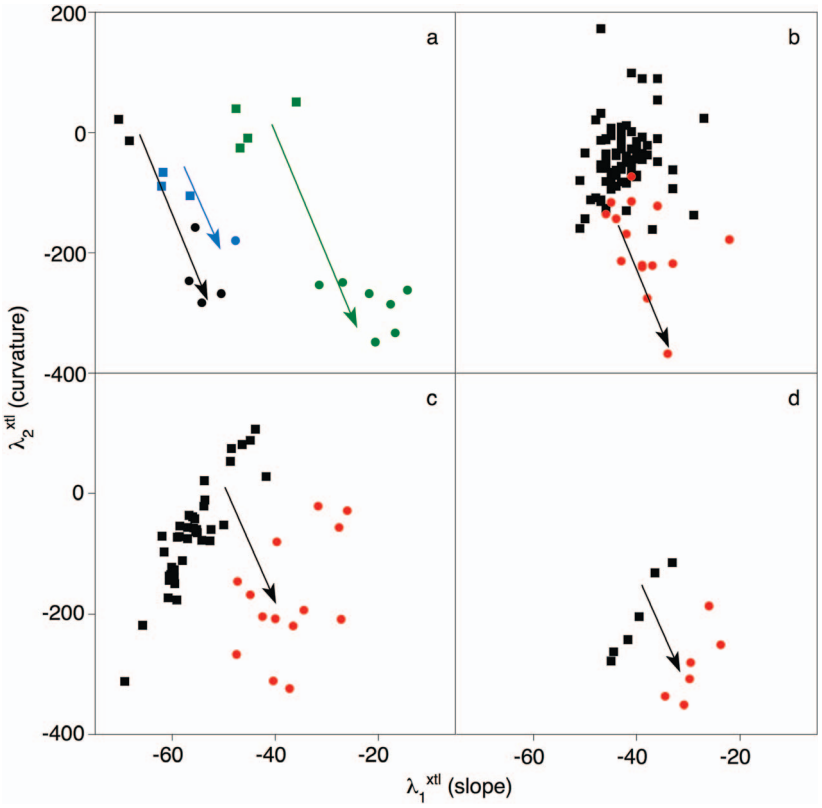

Fig. 6. The λ_2^{xtl} (curvature) and λ_1^{xtl} (slope) of zircons from (a) Val Malenco, Italy (black; Hermann & Rubatto, 2003), Seram, Indonesia (blue; Pownall et al., 2019) and the Betic Cordillera, Spain (green; Whitehouse & Platt, 2003), (b) the Lewisian Gneiss Complex, Scotland (MacDonald et al., 2015), (c) and (d) the Napier Complex, East Antartica (c, Taylor *et al.*, 2017 and d, Hokada & Harley, 2004). In all cases, older crystals or cores (squares) are seperated from younger crystals or rims (circles) in the direction of the garnet crystallisation vector.

datasets to be assessed by identifying λ_n^{xtl} from fits with high χ^2 as being potentially anomalous. It is of note that a random variation of 0.1 in REE contents results in very small changes to the λ_n^{xtl} (~0.1 in λ_0, 0.2 in λ_1, and 0.1 in λ_2).

The λ_1^{xtl} and λ_2^{xtl} for the zircons from Val Malenco (Italy), Seram (Indonesia), and the Betic Cordillera (Spain) are shown in Fig. 6a. The rims or overgrowths (circles; Fig. 6a) are separated from the cores (squares) in the direction of the garnet vector. This indicates that the new zircon growths record garnet crystallisation, in agreement with the original interpretations of the zircon REE patterns. The λ_n^{xtl} of the new overgrowths for the Val Malenco and Betic Cordillera zircon populations form 'groups' that are distinctly separate from the λ_n^{xtl} of the cores. This suggests that the new growths of zircon formed after garnet crystallisation rather than synchronously with garnet. This is consistent with the interpretation of the overgrowths from Val Malenco, as forming after garnet crystallisation (Hermann & Rubatto, 2003). The rims of zircons from the Betic Cordillera were interpreted to have grown during garnet formation, although only in the final stage of garnet growth (Whitehouse & Platt, 2003; Taylor *et al.*, 2017). The large separation between the λ_1^{xtl} and λ_2^{xtl} of the cores and rims of the Betic Cordillera zircons indicates that garnet had crystallised prior to the growth of the rims, while the spread in λ_1^{xtl} and λ_2^{xtl} of the Betic Cordillera rims could be due to continued garnet growth during their formation. Thus, the modelling is consistent with the original interpretation(s) of the zircon growth. The separation between the λ_1^{xtl} and λ_2^{xtl} of the cores and rims corresponds to the amount of garnet that has crystallised. This can be quantified and using the garnet partition coefficients at 900 °C (Fig. 3b) the core-rim separation corresponds to 20% garnet crystallisation for zircons from the Betic Cordillera. If these partition coefficients are multiplied by factors of 2 or 0.5, then the calculated amount of garnet that crystallised would change to 10% and 40%, respectively. This shows how changes in δ_n can be compensated by changes in the amount of crystallisation with little difference to the quality of fit (see Equation (3a) and (3b)). Thus, while the identification of garnet is largely independent of the partition coefficients selected (within the typical range), since the garnet vector always points in the same general direction, the approach should be used with caution for estimating the amount of crystallisation. In the present case, the Betic Cordillera zircons are hosted in a granulite containing 25% (by volume) garnet (Whitehouse & Platt, 2003).

The REE patterns and λ_1^{xtl} and λ_2^{xtl} of zircons from the Lewisian Gneiss Complex are shown in Figs S6 and 6b, respectively (MacDonald *et al.*, 2015). The Lewisian Gneiss Complex is principally composed of tonalite-trondhjemite-granodiorites that were metamorphosed to gneisses at amphibolite/granulite facies during the Archean and Proterozoic (MacDonald *et al.*, 2015). Subtle variations in REE pattern shape, which are not obvious in the REE patterns shown in Fig. S6, are distinguished by the λ_n enabling the identification of different zircon populations (Fig. 6b). The main group of zircons forms a cluster (black squares; Fig. 6b), while zircons hosted by two, locally associated, metasedimentary packages form a trend with the direction of the garnet crystal fractionation vector (red; Fig. 6b). Garnet is present in one of these metasedimentary packages and widely distributed in the locality of the other (MacDonald *et al.*, 2015). The metasedimentary zircons were suggested to be associated with a garnet-crystallising event due to their low Yb/Gd ratios (MacDonald *et al.*, 2015) and

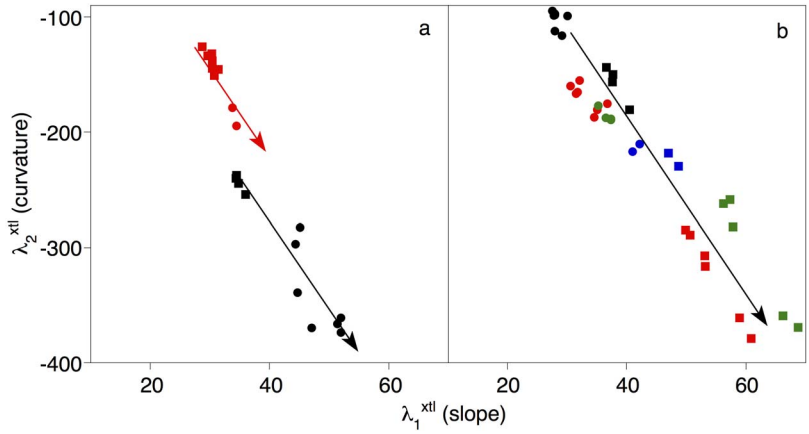

Fig. 7. The λ_2^{xtl} (curvature) and λ_1^{xtl} (slope) of monazite from (a) Val Malenco, Italy (black; Hermann & Rubatto, 2003) and Mount Stafford, Australia (red; Rubatto *et al.*, 2006), where crystal growths affected by garnet (circles) are separated from initial zones (squares) in the direction of the garnet crystallisation vector, and (b) the Himalayas, Bhutan (Warren *et al.*, 2018) hosted by different lithologies: metapelite LG-09-01 (black), schist LG-09-61 (blue), schist LG-09-90 (red), and schist LG-10-83 (green) where the cores (squares) crystallised in the presence of garnet; in this case, the garnet crystallisation vector is in the direction of rim to core.

the variation in λ_1^{xtl} and λ_2^{xtl} confirms this interpretation. The metasedimentary zircons are 2726–2506 Ma and their growth is attributed to the Archaean, granulite facies, Badcallian event at ~2700 Ma (MacDonald *et al.*, 2015). Garnet growth is believed to coincide with peak metamorphic conditions during this event (Zirkler *et al.*, 2012). As the continuous variation of λ_1^{xtl} and λ_2^{xtl} of the metasedimentary zircons indicates that they grew synchronously with garnet, the growth of these zircons can be correlated with peak metamorphism. Thus, in this case, the λ_1^{xtl} and λ_2^{xtl} not only confirm the association of these zircons with garnet but also enable the zircon growth to be related to a specific period of metamorphism.

The Napier Complex in East Antarctica is composed of granulite facies, ultra-high-temperature tonalitic to granitic gneisses (Hokada & Harley, 2004; Kelly & Harley, 2005; Kusiak *et al.*, 2013; Taylor *et al.*, 2017). The complex has undergone at least two major metamorphic events dated at 2800 and 2500 Ma. The λ_n of zircons from garnet-bearing gneiss (Taylor *et al.*, 2017) and a leucosome-rich garnet bearing gneiss/quartzite (Hokada & Harley, 2004) were determined and are shown in Fig. 6. The positive correlation between λ_1^{xtl} and λ_2^{xtl} (particularly well exhibited by zircons >2500 Ma; black population in Fig. 6c) is characteristic of all REE pattern datasets (O'Neill, 2016) but could also be caused by the crystallisation of amphibole or clinopyroxene. The λ_1^{xtl} and λ_2^{xtl} 'intrinsic' correlation and a trend caused by amphibole/clinopyroxene crystallisation can be distinguished if the petrology of the host rock is known as the large amount of crystallisation (>80%) necessary for an observable trend means that amphibole or clinopyroxene would have to be a major mineral. The REE contents of zircons younger than 2500 Ma from the garnet-bearing gneiss were considered to be in equilibrium with garnet (Taylor *et al.*, 2017). The displacement of the λ_1^{xtl} and λ_2^{xtl} of zircons younger than 2500 Ma (red circles; Fig. 6c) from older zircons (black squares; Fig. 6c) in the direction of the garnet crystallisation vector is consistent with this interpretation. The rims of the zircons from the leucosome-rich garnet bearing gneiss/quartzite were considered to have grown synchronously with garnet (Hokada & Harley, 2004). In contrast, Taylor *et al.* (2017) reinterpreted the zircon REE patterns and suggested that the zircon cores rather than the rims were in equilibrium with garnet. The λ_1^{xtl} and λ_2^{xtl} of neither the zircon cores nor rims align along the garnet vector indicating that neither crystallised synchronously with garnet. However, the λ_1^{xtl} and λ_2^{xtl} of the rims are separated from the λ_1^{xtl} and λ_2^{xtl} of the cores in the direction of the garnet crystallisation vector (Fig. 6d), indicating that the zircon rims formed after garnet crystallisation. The λ_1^{xtl} and λ_2^{xtl} of the zircon cores (black squares; Fig. 6d) are more similar to the zircons from the garnet-bearing gneiss that crystallised after (red circles; Fig. 6c) rather than prior (black squares; Fig. 6c) to garnet crystallisation. This indicates that the zircon cores grew from a system that was relatively depleted in the HREE, which could be due the prior crystallisation of garnet. Thus, the λ_1^{xtl} and λ_2^{xtl} of the zircons from the leucosome-rich garnet bearing gneiss/quartzite suggest four evolutionary stages: (1) the development of a HREE-depleted melt possibly due to garnet crystallisation, (2) crystallisation of the zircon cores, (3) garnet crystallisation, and (4) crystallisation of the zircon rims. This model explains the contrasting interpretations of Hokada & Harley (2004) and Taylor *et al.* (2017) with both the zircon rims and cores having grown from HREE-depleted melts.

The ability of monazite to similarly record and identify metamorphic events was also investigated. Monazite crystals from Val Malenco, Italy (Hermann & Rubatto, 2003; that formed alongside the Val Malenco zircons), Mount Stafford, Australia (Rubatto *et al.*, 2006), and the Himalayas, Bhutan (Warren *et al.*, 2018), which all have growth zones associated with garnet crystallisation, were selected. The REE data used are reproduced from their original sources in Table S3. The REE monazite patterns were fit to the orthogonal polynomials and the λ_1^{xtl} and λ_2^{xtl} determined from the fits are given in Table S3 and shown in Fig. 7. The λ_1^{xtl} and λ_2^{xtl} of monazite define trends (Fig. 7) that are consistent with the crystallisation of garnet (Fig. 2). This shows that the variation in REE contents of monazite can also be related to the crystallisation of other REE-bearing minerals.

The monazite crystals from the Himalayas are hosted by metapelites that experienced sub-solidus amphibolite facies metamorphism (Warren *et al.*, 2018). The cores of these crystals are considered to have crystallised synchronously with garnet, as monazite inclusions are present in the garnet crystals, while the rims are believed to have formed during garnet breakdown due to their high Y and HREE contents (Warren *et al.*, 2018). The high values of λ_1^{xtl} and strongly negative values of λ_2^{xtl} of many of the monazite cores (Fig. 7b) are consistent with their co-crystallisation with garnet (Fig. 7a). The λ_1^{xtl} and λ_2^{xtl} of the

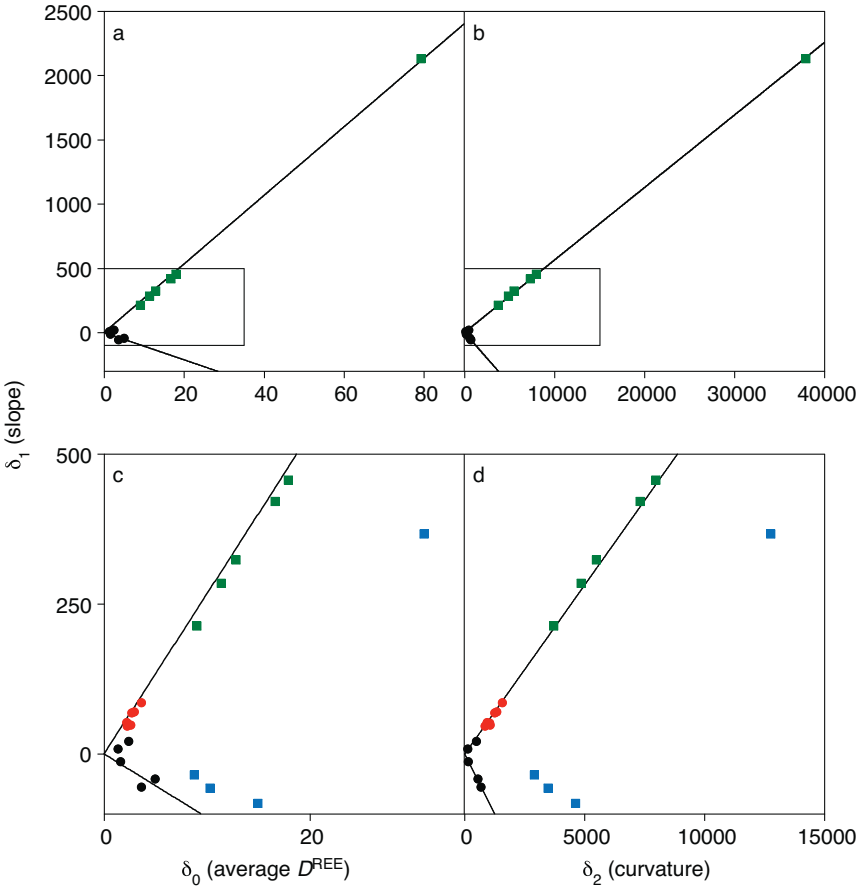

Fig. 8. The δ_1 (slope) vs (a, c) δ_0 (average D^{REE}) and (b, d) δ_2 (curvature) for equilibrium zircon/garnet D^{REE} determined at 800–1000 °C and 0.2 GPa (black circles; Rubatto & Hermann, 2007) and 900–1000 °C and 0.7 GPa (green squares; Taylor *et al.*, 2015) and zircon rim/garnet rim (red circles) and zircon core/garnet rim (blue squares) for zircon and garnet from the Betic Cordillera (Whitehouse & Platt, 2003), (c) and (d) correspond to the insets shown in (a) and (b), respectively. The δ_0, δ_1, and δ_2 of the equilibrium zircon/garnet D^{REE} form linear arrays (the linear best fits, constrained to go through 0, 0 are shown as solid lines), which change direction around $\delta_1 = 0$ as the constant form of the f_1 orthogonal polynomial causes the coefficient to change sign.

rims are separated from the λ_1^{xtl} and λ_2^{xtl} of the cores in the direction of the monazite crystallisation vector (Fig. 2), suggesting that the change in λ_1^{xtl} and λ_2^{xtl} from the monazite cores to the rims could simply be due to the crystallisation of monazite rather than the breakdown of garnet. The crystallisation of monazite causes a depletion of the LREE in the residual (Fig. 5c) and the REE patterns of minerals crystallising alongside monazite should be progressively depleted in the LREE as crystallisation proceeds (Fig. 5d). However, an enrichment of the HREE rather than a depletion in the LREE of the rims relative to the cores is observed (see Fig. 4 in Warren *et al.*, 2018). Further, the crystallisation of monazite should cause a depletion of the REE ($\delta_0 > 1$; Supplementary Data), whereas the λ_0^{xtl} of the monazite cores and rims are relatively constant at 9.9(7) (Table S3). Thus, in this case, the λ_0^{xtl} of the cores and rims are important for constraining the growth history of the different monazite zones.

Applicability of λ_n modelling

Constant values of D^{REE} were used in the models for simplicity, however, D^{REE} may not be constant during an anatectic event due to changes in temperature, pressure and/or composition. The crystal site onto which the REE partition is the primary control on the shape of D^{REE} patterns and hence changes in crystallisation conditions do not significantly affect the direction of the vectors (Figs 2, 3, and 4b). This suggests that if a mineral was to crystallise from a closed system that undergoes multiple changes in temperature, pressure, and 'participating' composition, then the shape terms of the residual pattern would simply scatter around the linear trend modelled for constant D^{REE}. The λ_n of zircon and monazite that are associated with garnet crystallisation show some level of scatter but generally align along a linear trend (Figs 6 and 7), consistent with this hypothesis.

The models presented here assume that equilibrium is reached, which is very likely to be the case when a mineral grows from a melt or fluid. However, the REE contents of a mineral may not be in equilibrium with the surrounding system during sub-solidus growth and could reflect the different diffusion rates of the REE (e.g. Skora *et al.*, 2006; Gervais & Crowley, 2017; Holder *et al.*, 2018). The problem of disequilibrium is inherent to the use of trace element contents to interpret sub-solidus conditions, as not only would the modelling presented here not be applicable, but ratios such as La/Sm and Yb/Gd would also not be meaningful to interpret. Thus, in cases of disequilibrium it would be difficult, if not impossible, to use the REE contents of minerals as petrogenetic indicators. However, in cases of partial equilibrium, it is likely that the REE content of a mineral will record changes in the system in the manner modelled, albeit with some scatter around the modelled trends. Indeed, for the zircon and monazite REE patterns investigated the effects of any disequilibrium appear to be less important than the bulk-compositional effect of garnet fractional crystallisation.

The synchronous growth of garnet and zircon can be identified by comparing the zircon/garnet D^{REE} of a sample to zircon/garnet D^{REE} determined when garnet and zircon are known to have grown in equilibrium. If the shape of the zircon/garnet D^{REE} matches that of the equilibrium zircon/garnet D^{REE}, then the garnet and zircon REE contents can be considered to be in equilibrium (e.g. Rubatto, 2002; Hermann & Rubatto, 2003; Whitehouse & Platt, 2003) and the two minerals will have grown contemporaneously. Taylor *et al.* (2017) parameterised the shape of zircon/garnet D^{REE} in terms of D^{Yb} (i.e. HREE concentration) and $D^{Yb/Gd}$ (i.e. HREE/MREE slope) and showed that when in equilibrium $\log(D^{Yb})$ vs $\log(D^{Yb/Gd})$ forms a linear array as a function of pressure and temperature. The zircon/garnet $\log(D^{Yb})$ and $\log(D^{Yb/Gd})$ for a sample can then be compared with this array to determine whether or not the zircon and garnet are in equilibrium (Taylor *et al.*, 2017). The shape of zircon/garnet D^{REE} can also be parameterised in terms of δ_0 (average D^{REE}), δ_1 (slope), and δ_2 (curvature) (see Equation (2a)), which similarly forms linear arrays for samples in equilibrium (Fig. 8a and b), enabling an assessment of equilibrium for unknown samples. As an example, zircon/garnet δ_n determined using the zircon REE contents in Table S2 and the garnet REE content of sample gt-B-r Rim in Table 2 of Whitehouse & Platt, 2003, from the Betic Cordillera, are shown in Fig. 8c and d. REE data for multiple zircons but a single garnet were used in keeping with the approach of Taylor *et al.* (2017). The zircon rims are in equilibrium with the garnet rim and lie on the equilibrium arrays (red; Fig. 8c and d), while the cores are not in equilibrium with the garnet rim and hence do not lie on the equilibrium arrays (blue; Fig. 8c and d). This is consistent with the λ_n of the zircon REE patterns, which show that the rims crystallised synchronously with garnet (green; Fig. 6a). This method for identifying the synchronous growth of zircon and garnet is primarily a test of equilibrium and differs to that of the λ_n approach presented here, for which the main purpose is to determine the relative timing of mineral growth. Further, the λ_n approach can be applied to other minerals (e.g. monazite) and enables in theory, the synchronous growth of any REE-bearing mineral with any other REE-bearing mineral to be identified and is not limited to systems for which mineral/mineral D^{REE} have been determined.

CONCLUSION

The shapes of REE patterns can be quantified by fitting the REE concentrations, which vary as a function of ionic radius, to orthogonal polynomials. Changes in the REE pattern shape of zircon due to the crystallisation of other REE bearing phases can be modelled, enabling phases that crystallised after, synchronously with, and prior to the growth of zircon to be identified. This modelling can also be applied to the REE patterns of other phases, such as monazite. The approach is an improvement on the qualitative assessment of differences in REE patterns as it allows changes in shape to be quantified. Further, while the slope parameter (λ_1^{xtl}) provides a similar parameterisation of REE pattern shape as REE ratios such as La/Sm and Yb/Gd, the use of all the REE to parameterise slope means that it is less susceptible to the effects of LREE-contamination or analytical artefacts (which appear to affect Sm and Gd disproportionately relative to the other REE; O'Neill, 2016). The use of a parameter for curvature in conjunction with a slope parameter further improves the ability to discern differences in the shape of REE patterns. An additional advantage of the shape parameters described here is that they enable the relative timing of mineral crystallisation to be determined (Fig. 6), allowing dated zircon growths to be correlated with specific metamorphic (e.g. garnet-forming) events. Parameterising the shape of REE patterns in terms of λ_n represents a new tool that can be used in conjunction with other trace element data (e.g. U/Th ratios and Eu anomalies) to construct detailed histories of complex terranes.

DATA AVAILABILITY

The data used in this article are available in its online supplementary material.

FUNDING

This research was supported by the Australian Research Council (FL160100168).

ACKNOWLEDGEMENTS

We thank Clare Warren, Robert Holder, and Simon Harley for their reviews of the manuscript and Jörg Hermann for his editorial handling.

References

Anenburg, M. (2020). Rare earth mineral diversity controlled by REE pattern shapes. *Mineralogical Magazine* **84**, 629–639. https://doi.org/10.1180/mgm.2020.70.

Burnham, A. D. (2020). Key concepts in interpreting the concentrations of the rare earth elements in zircon. *Chemical Geology* **551**, 119765. https://doi.org/10.1016/j.chemgeo.2020.119765.

Burnham, A. D. & Berry, A. J. (2012). An experimental study of trace element partitioning between zircon and melt as a function of oxygen fugacity. *Geochimica et Cosmochimica Acta* **95**, 196–212. https://doi.org/10.1016/j.gca.2012.07.034.

Burnham, A. D. & Berry, A. J. (2017). Formation of Hadean granites by melting of igneous crust. *Nature Geoscience* **10**, 457–461. https://doi.org/10.1038/ngeo2942.

Claiborne, L. L., Miller, C. F., Gualda, G. A. R., Carley, T. L., Covey, A. K., Wooden, J. L. & Fleming, M. A. (2018) Zircon as magma monitor: robust, temperature-dependent partition coefficients from glass and zircon surface and rim measurements from natural systems. In: Moser D. E., Corfu F., Darling J. R., Reddy S. M. & Tait K. (eds) *Microstructural Geochronology: Planetary Records Down to Atom Scale*, 1st edn. Geophysical Monograph 232, John Wiley & Sons, pp. 3–33. https://doi.org/10.1002/9781119227250.ch1.

Crowley, J. L., Myers, J. S. & Dunning, G. R. (2006). Timing and nature of multiple 3700-3600 Ma tectonic events in intrusive rocks north of the Isua greenstone belt, southern West Greenland. *GSA Bulletin* **114**, 1311–1325. https://doi.org/10.1130/0016-7606(2002)114<1311:TANOMM>2.0.CO;2.

Gervais, F. & Crowley, J. L. (2017). Prograde and near-peak zircon growth in a migmatitic pelitic schist of the southeastern Canadian Cordillera. *Lithos* **282–283**, 65–81. https://doi.org/10.1016/j.lithos.2017.02.016.

Goodenough, K. M., Crowley, Q., Krabbendam, M. & Parry, S. F. (2013). New U-Pb age constraints for the Laxford Shear Zone, NW Scotland: evidence for tectono-magmatic processes associated with the formation of a Palaeoproterozoic supercontinent. *Precambrian Research* **233**, 1–19. https://doi.org/10.1016/j.precamres.2013.04.010.

Hermann, J. & Rubatto, D. (2003). Relating zircon and monazite domains to garnet growth zones: age and duration of granulite facies metamorphism in the Val Malenco lower crust. *Journal of Metamorphic Geology* **21**, 833–852. https://doi.org/10.1046/j.1525-1314.2003.00484.x.

Hokada, T. & Harley, S. L. (2004). Zircon growth in UHT leucosome: constraints from zircon-garnet rare earth elements (REE) relations in Napier Complex, East Antarctica. *Journal of Mineralogical and Petrological Sciences* **99**, 80–190. https://doi.org/10.2465/jmps.99.180.

Holder, R. M., Hacker, B. R., Horton, F. & Rakotondrazafy, A. M. (2018). Ultrahigh-temperature osumilite gneisses in southern Madagascar record combined heat advection and high rates of radiogenic heat production in a long-lived high-T orogen. *Journal of Metamorphic Geology* **36**, 855–880. https://doi.org/10.1111/jmg.12316.

Hopkins, M., Harrison, T. M. & Manning, C. E. (2008). Low heat flow inferred from >4 Gyr zircons suggest hadean boundary interactions. *Nature* **456**, 493–496. https://doi.org/10.1038/nature07465.

Kelly, N. M. & Harley, S. L. (2005). An integrated microtextural and chemical approach to zircon geochronology: refining the Archaean history of the Napier complex, East Antarctica. *Contributions to Mineralogy and Petrology* **149**, 57–84. https://doi.org/10.1007/s00410-004-0635-6.

Kusiak, M. A., Whitehouse, M. J., Wilde, S. A. , Dunkley, D. J., Menneken, M. J., Nemchin, A. A. & Clark, C. (2013). Changes in zircon chemistry during Archean UHT metamorphism in the Napier Complex, Antarctica. *American Journal of Science* **313**, 933–967. https://doi.org/10.2475/09.2013.05.

MacDonald, J. M., Goodenough, K. M., Wheeler, J., Crowley, Q., Harley, S. L., Mariani, E. & Tatham, D. (2015). Temperature–time evolution of the Assynt terrane of the Lewisian Gneiss Complex of Northwest Scotland from zircon U-Pb dating and Ti thermometry. *Precambrian Research* **260**, 55–75. https://doi.org/10.1016/j.precamres.2015.01.009.

Miller, L. A., O'Neill, H. S. C., Berry, A. J. & Le Losq, C. (2022). Fractional crystallisation of eclogite during the birth of a Hawaiian Volcano. *Nature Communications* **13**, 1–8. https://doi.org/10.1038/s41467-022-30108-x.

Moyen, J. F. (2011). The composite Archaean grey gneisses: petrological significance, and evidence for a non-unique tectonic setting for Archaean crustal growth. *Lithos* **123**, 21–36. https://doi.org/10.1016/j.lithos.2010.09.015.

Nutman, A. P., Friend, C. R. & Bennett, V. C. (2002). Evidence for 3650–3600 Ma assembly of the northern end of the Itsaq Gneiss Complex, Greenland: implication for early Archaean tectonics. *Tectonics* **21**, 5-1–5-28. https://doi.org/10.1029/2000TC001203

O'Neill, H. S. C. (2016). The smoothness and shapes of chondrite-normalized rare earth element patterns in basalts. *Journal of Petrology* **57**, 1463–1508. https://doi.org/10.1093/petrology/egw047.

Pownall, J. M., Hall, R., Armstrong, R. A. & Forster, M. A. (2014). Earth's youngest known ultrahigh-temperature granulites discovered on Seram, eastern Indonesia. *Geology* **42**, 279–282. https://doi.org/10.1130/G35230.1.

Pownall, J. M., Armstrong, R. A., Williams, I. S., Thirlwall, M. F., Manning, C. J. & Hall, R. (2019). Miocene UHT granulites from Seram, eastern Indonesia: a geochronological–REE study of zircon, monazite and garnet. *Geological Society, London, Special Publications* **478**, 167–196. https://doi.org/10.1144/SP478.8.

Reimink, J. R., Chako, T., Stern, R. A. & Heaman, L. M. (2014). Earth's earliest evolved crust generated in an Iceland-like setting. *Nature Geoscience* **7**, 529–533. https://doi.org/10.1038/ngeo2170.

Rubatto, D. (2002). Zircon trace element geochemistry: partitioning with garnet and the link between U–Pb ages and metamorphism. *Chemical Geology* **184**, 123–138. https://doi.org/10.1016/S0009-2541(01)00355-2.

Rubatto, D. (2017). Zircon: the metamorphic mineral. *Reviews in Mineralogy and Geochemistry* **83**, 261–295. https://doi.org/10.2138/rmg.2017.83.9.

Rubatto, D. & Hermann, J. (2007). Experimental zircon/melt and zircon/garnet trace element partitioning and implications for the geochronology of crustal rocks. *Chemical Geology* **241**, 38–61. https://doi.org/10.1016/j.chemgeo.2007.01.027.

Rubatto, D., Hermann, J. & Buick, I. S. (2006). Temperature and bulk composition control on the growth of monazite and zircon during low-pressure anatexis (Mount Stafford, Central Australia). *Journal of Petrology* **47**, 1973–1996. https://doi.org/10.1093/petrology/egl033.

Schaltegger, U., Fanning, C. M., Günther, D., Maurin, J. C., Schulmann, K. & Gebauer, D. (1999). Growth, annealing and recrystallization of zircon and preservation of monazite in high-grade metamorphism: conventional and in-situ U-Pb isotope, cathodoluminescence and microchemical evidence. *Contributions to Mineralogy and Petrology* **134**, 186–201. https://doi.org/10.1007/s004100050478.

Shaw, D. M. (2006). *Trace Elements in Magmas: a Theoretical Treatment*. Cambridge University Press.

Skora, S., Baumgartner, L. P., Mahlen, N. J., Johnson, C. M., Pilet, S. & Hellebrand, E. (2006). Diffusion-limited REE uptake by eclogite garnets and its consequences for Lu-Hf and Sm-Nd geochronology. *Contributions to Mineralogy and Petrology* **152**, 703–720. https://doi.org/10.1007/s00410-006-0128-x.

Sutton, J. & Watson, J. V. (1951). The pre-Torridonian metamorphic history of the Loch Torridon and Scourie areas in the NW Highlands and its bearing on the chronological classification of the Lewisian. *Journal of the Geological Society, London* **106**, 241–308.

Taylor, R. J. M., Harley, S. L., Hinton, R. W., Elphick, S., Clark, C. & Kelly, N. M. (2015). Experimental determination of REE partition coefficients between zircon, garnet and melt: a key to understanding high-T crustal processes. *Journal of Metamorphic Geology* **33**, 231–248. https://doi.org/10.1111/jmg.12118.

Taylor, R. J. M., Clark, C., Harley, S. L., Kylander-Clark, A. R. C., Hacker, B. R. & Kinny, P. D. (2017). Interpreting granulite facies events through rare earth element partitioning arrays. *Journal of Metamorphic Geology* **35**, 759–775. https://doi.org/10.1111/jmg.12254.

Warren, C. J., Greenwood, L. V., Argles, T. W., Roberts, N. M., Parrish, R. R. & Harris, N. B. (2018). Garnet-monazite rare earth element relationships in sub-solidus metapelites: a case study from Bhutan. *Geological Society, London, Special Publications* **478**, 145–166. https://doi.org/10.1144/SP478.1.

Wheeler, J., Park, R. G., Rollinson, H. R. & Beach, A. (2010) The Lewisian complex: insights into deep crustal evolution. In: Law R. D., Butler R. W. H., Holdsworth R. E., Krabbendam M. & Strachan R. A. (eds) *Continental Tectonics and Mountain Building*, vol. 335. The Geological Society Publishing House, London, pp. 51–79.

Whitehouse, M. J. & Platt, J. P. (2003). Dating high-grade metamorphism-constraints from rare-earth elements in zircon and garnet. *Contributions to Mineralogy and Petrology* **145**, 61–74. https://doi.org/10.1007/s00410-002-0432-z.

Wood, B. J. & Blundy, J. D. (2014) Trace element partitioning: the influenced of ionic radius, cation charge, pressure and temperature. In: Holland H. D. & Turekian K. K. (eds) *Treatise on Geochemistry*, vol. 3, 2nd edn. Elsevier, pp. 421–448.

Yakymchuk, C. & Brown, M. (2014). Behaviour of zircon and monazite during crustal melting. *Journal of the Geological Society* **171**, 465–479. https://doi.org/10.1144/jgs2013-115.

Zirkler, A., Johnson, T. E., White, R. W. & Zack, T. (2012). Polymetamorphism in the mainland Lewisian complex, NW Scotland phase equilibria and geochronological constraints from the Cnoc an t'Sidhean suite. *Journal of Metamorphic Geology* **30**, 865–885. https://doi.org/10.1111/j.1525-1314.2012.01003.x.

Deltech Furnaces

Sustained operating temperatures to 1800° Celsius

www.deltechfurnaces.com

Gas Mixing System

An ISO 9001:2015 certified company

Custom Vertical Tube

ASME NQA-1 2008 Nuclear Quality Assurance

Standard Vertical Tube

Control systems are certified by Intertek UL508A compliant

Bottom Loading Vertical Tube